INPAINTING THE SINOGRAM FROM COMPUTED TOMOGRAPHY USING LATENT DIFFUSION MODEL AND PHYSICS

Anonymous authors
Paper under double-blind review

ABSTRACT

Computed Tomography (CT) is a widely used non-invasive imaging technique for materials at microscopic or sub-microscopic length scales in synchrotron radiation facilities. Typically, the object is rotated relative to the X-ray beam, and 2D projection images are recorded by the detector at different rotation angles. The 3D object is then reconstructed by combining these projections and solving a computationally demanding inverse problem. The quality of the reconstructed image is critical for scientific analysis and is influenced by various factors, including the number of projections, exposure time or dose, and the reconstruction algorithm. In this work, we develop a foundation model by integrating a Generative AI-based Latent Diffusion Model (LDM) with physics-based domain knowledge. Specifically, we first develop and incorporate a set of loss functions into our LDM that accurately capture the physical properties of the CT data acquisition process. We demonstrate that adding these loss functions aids in stable training of the autoencoder in the LDM and improves its accuracy. The autoencoder and the diffusion model of the LDM are trained with real-world experimental data. Collecting real-world experimental data from synchrotron beamlines is often time-consuming and challenging. We demonstrate that the autoencoder trained with a combination of real-world experimental data and phantom shapes features also performs similarly to the autoencoder trained with real-world data. Second, we introduce a novel image blending method to combine the LDM's generated output with the original, extremely sparse sinogram data. Since our model integrates physics-guided loss functions focused on CT data acquisition, it simplifies the creation of downstream tasks and facilitates the adaptation of new features from different experiments. We demonstrate improvements of up to 23.5% in SSIM for sinogram quality and 13.8% for reconstructed image quality compared to state-of-the-art techniques.

1 INTRODUCTION

X-ray computed tomography (XCT) is a common and widely used non-invasive imaging technique at the synchrotron light sources (Sedigh Rahimabadi et al., 2020). XCT is used for many domain sciences, including imaging materials (Tang et al., 2021; Zhao et al., 2024; Intelligence Advanced Research Projects Activity), biological materials Keklikoglou et al. (2021), and others (Advanced Photon Source, Argonne National Laboratory). In a XCT experiment at the synchrotron beamlines,
parallel X-ray beam is incident on an object placed on a rotation stage and rotated at different angles. R4−Q1b−A
For each rotation angle, the transmitted projection images are recorded in the detector based on the R4−Q1c−A
experimental geometrical configuration and alignment (Dyer et al., 2017), as shown in Fig. 1 . This
is the focus use case in this work. Unlike medical/laboratory systems, synchrotron radiation facilities R2−W3−A
mostly use parallel beam geometry due to higher spatial and temporal resolution requirements. In R2−Q3−A
medical/laboratory systems, typically the patient/object is stationary, with the source and detector rotating around the patient. We are not alluding to such medical experiments in this work.

The projection images can also be represented in terms of sinogram just by transposing the x or y
coordinates of the projection image with that by the projection angle. Subsequently after all these R4−Q1d−A
projection images have been collected, a reconstruction algorithm is used that utilizes all these images to reconstruct the 3D object at high resolution. The quality of the reconstruction is essential

for understanding the morphology and properties of the material and advancing scientific reasoning. Typically, to obtain high-quality 3D reconstruction, data is collected along a densely sampled tra-

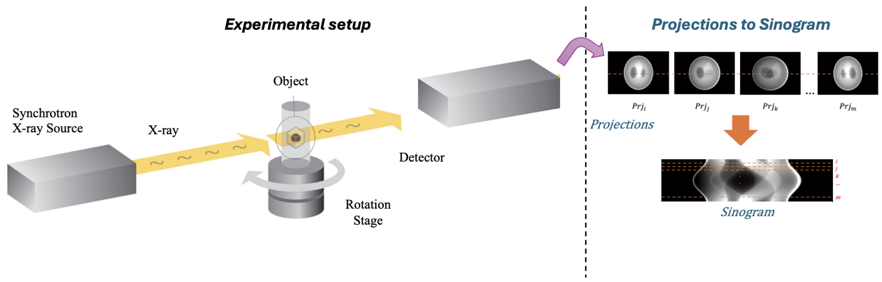

Figure 1: X-ray data acquisition schematic in a synchrotron beamline facility.

jectory during a CT experiment. However, this process is time-consuming – requiring hours or even days. Synchrotron radiation facilities provide high-energy X-rays that enable XCT experiments with high spatial and temporal resolutions. However, such high-energy beams also translate to a high radiation dose on the sample, which can easily deform small features, especially when coupled with extended data acquisition times. In order to alleviate these issues , the data acquisition approach is often modified, leading to sparse measurements. In one approach, the number of acquired projections is randomly reduced. In the second approach, the projection images are acquired sparsely at equal intervals, which leads to angular undersampling, referred to as the sparse view (SV) problem. In a third approach, driven by geometric limitations of the rotation stage, there can be a range of angles where projections cannot be acquired - often referred to as the missing wedge or limited angle (LA) problem. Other incomplete projection data involves metal-corrupted projections, interior tomography problem and non-uniform detector problem (Wang et al., 2023). In this work, we address the SV and LA problems, where there are lack of projections results in band-like missing patterns in the sinogram, as shown in the input of stage-1 of the LDM in Fig. 2.

R4−Q1e−A
R4−Q1b−A
R4−Q1f−A
R4−Q1f−A

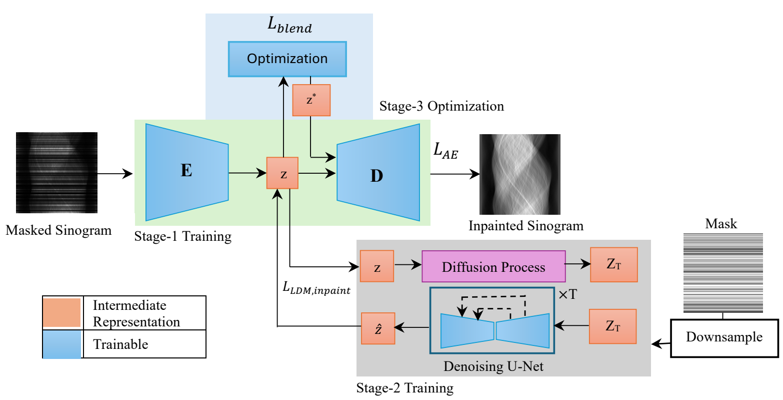

Figure 2: Overview of our algorithm. Stage-1 training: the autoencoder of the LDM is trained with a novel addition of physics-driven losses. Stage-2 training: the diffusion part of the LDM is trained. Stage-3: an optimization is done to blend the unmasked sinogram and the LDM prediction. R3−Q2−A

In this paper, we improve the sparse data CT to dense data CT by inpainting the sinogram in the measurement domain, using our algorithm shown in Fig. 2. We develop a novel DL method with Generative AI-based LDM. The model is fed with missing sinogram data and the missing regions as masks. The LDM performs the task of sinogram inpainting and generates a sinogram with the filled information in the missing regions. The loss function of the autoencoder in the LDM is further improved with the domain-specific physics loss functions. In particular, we leverage the image formation process in the measurement and reconstructed object domains via the new loss function. Subsequently, we incorporate a novel blending algorithm to blend the output of the LDM with the original sparse data. The entire model is trained and tested with real-world datasets and shows a significant improvement in image quality. Lastly, since our model is trained in the sinogram domain with a significant variety and volume of synchrotron radiation experimental data, it can be used as a foundation model for CT experiments and meet the requirements of many downstream ML tasks. We demonstrate this capability with LA and extremely sparse SV tasks. **Specifically, we make the following contributions: (1)** we develop a novel method of training the autoencoder in LDM by adding domain-specific physics knowledge of CT image formation for inpainting sinograms taking into account both measurement and reconstruction domains, which shows training stability of the autoencoder trained in an adversarial manner; **(2)** we develop a novel blending algorithm that improves the accuracy of inpainting tasks; **(3)** we develop two downstream tasks that address the SV and LA artifacts. Our downstream tasks use our foundation model which is trained with random masking; **(4)** we demonstrate the benefits of our approach for real-world tomographic data.

2 RELATED WORK

Various object reconstruction and analysis algorithms have been developed for limited CT data. The classical method of direct reconstruction from sinogram uses Filtered Backprojection (FBP) algorithm by Kak & Slaney (2001). However, FBP causes lot of artifacts in the CT reconstruction with limited projections. A Fourier grid reconstruction algorithm, Gridrec offers computational R4−Q1d−A efficiency and less artifacts (Dowd et al., 1999; Rivers, 2012). Other approach is to address this ill-posed problem with iterative reconstruction algorithms such as Simultaneous Iterative Reconstruction Technique (SIRT) (Gilbert, 1972; Herman & Lent, 1976a;b; Van der Sluis & Van der Vorst, 1990), Simultaneous Algebraic Reconstruction Technique (SART) (Andersen & Kak, 1984), Discrete R2−W5−A Algebraic Reconstruction Technique (DART) (Batenburg & Sijbers, 2011), Model-Based Iterative Reconstruction (MBIR)(Venkatakrishnan et al., 2014), Low-tilt Tomographic Reconstruction (LoTToR) (Zhai et al., 2020) and others. Although these methods can reduce image noise and artifacts, R1−W1−A the reconstruction results are unsatisfactory without prior image information. A constrained total variation (TV) based iterative image reconstruction algorithm has also been developed (Sidky & Pan, 2008). Despite effectiveness of TV regularization in preserving edge and restoring smooth regions, fine features and image details are often overlooked. Another method of solving this problem using data-fidelity term with appropriate priors has been done (Kudo et al., 2013; Vandeghinste et al., 2011; Zhu et al., 2013). An alternative approach is to solve this problem as inpainting problem R1−W1−A in the sinogram domain has the advantage of not suffering from aliasing artifacts.

Deep learning (DL)-based reconstruction algorithms have been popular in recent years, aiming to solve this limited CT problem. In this realm, GANs (Goodfellow et al., 2014; Valat et al., 2023) and U-Nets (Ronneberger et al., 2015) perform relatively well by considering the entire sinogram (Dong et al., 2019; Ghani & Karl, 2018; Tan et al., 2019; Yoo et al., 2019) or the local regions (Lee et al., 2018). One of the first to incorporate measurement and reconstruction domains by adding an inverse Radon transform layer is shown by Würfl et al. (2016). Approaches relevant to CT applications combining data from sinograms as well as reconstructed image domains are also used. An unsupervised sinogram inpainting network trained in both these domains has been shown by Zhao et al. (2018) for LA tomography. Similar principles of dual modalities in CT metal artifact reduction were presented by Lin et al. (2019) for removing metal artifacts and refining object reconstruction. The use of perceptual loss in networks has been presented in (Wei et al., 2020; Wu et al., 2020; Liu et al., 2020). A novel loss function and framework in both sinogram and image domain in a 2-step network for reconstruction from SV CT is presented by Wei et al. (2020). The use of local and global losses in the sinogram and residual error between reconstructed images has been presented by Yang et al. (2022). In Wu et al. (2021), reconstruction from SV CT has been done with the model consisting of embedding, refinement, and awareness modules. A similar R2−W4−A approach by Ding et al. (2021) performs computationally efficient CT image reconstruction from SV CT in discrete Fourier domain. Adler & Öktem (2017) uses a gradient-like scheme while using prior information to solve the ill-posed inverse problem of CT reconstruction. Works such as Kofler et al. (2018) use a cascade of U-nets and data consistency layers to solve the SV CT problem, and the LA problem in CT as well (Yao et al., 2024). In recent years, Transformer (Dosovitskiy et al., 2020) architectures have been applied for the task of sparse CT upsampling. A Dense Residual Hierarchical Transformer network with attention-weighted loss is presented for sinogram inpainting by Adishesha et al. (2023). A transformer-based masked sinogram model for ill-posed problems is addressed in Liu et al. (2022). All these DL methods often omit the consistency of measured data and result in the inaccurate representation of the image structure and features.

ADMM based DL approaches has been used for reconstructions from LA CT (Wang et al., 2019) R2−W5−A and SV CT (Wang et al., 2022) which automatically adjusts the regularization. Such approaches are iterative algorithms with sensitivity to the training data. Combining iterative reconstruction with DL under the plug-and-play (PnP) framework have also been explored which adaptively learns the image priors to represent complex features and structures, while enhancing the reconstruction quality (Ye et al., 2018; Kamilov et al., 2023; He et al., 2019). PnP methods typically do not simultaneously consider local and nonlocal prior knowledge and is sensitive to the chosen denoiser. These DL based approaches (including ADMM and PnP) are often trained with limited features which limits its use for diverse applications. In E et al. (2024), a novel algorithm for inpainting of CT data based on LDM with the Fourier transform augmented autoencoder is presented. However, the work focuses on randomly masked projections, and does not demonstrate its feasibility to LA and SV tasks.

In general image inpainting tasks, a novel attention-based network (transformer) for image inpainting, based on an hourglass-shaped attention structure to generate appropriate features for complemented images is introduced by Deng et al. (2022). This paper also introduces Laplace attention based on Laplace distance prior for vanilla multi-attention head. A novel continuous-mask-aware transformer for image inpainting using masked attention and overlapping tokens is introduced by Ko & Kim (2023). A multi-level interactive Siamese filtering for inpainting of high-fidelity image inpainting has been proposed Li et al. (2022). To increase the receptive field in the inpainting network, Fourier Convolutions have been introduced Suvorov et al. (2022). Tackling semantic discrepancy in Diffusion Models for image inpainting to facilitate consistent and meaningful semantic generation has been introduced by Liu et al. (2024). CoPaint is introduced in Zhang et al. (2023), which can coherently inpaint the whole image without introducing mismatches. In Lugmayr et al. (2022), a novel algorithm RePaint is introduced. It uses the Denoising Diffusion Probabilistic Model (DDPM) for inpainting even in extreme masks. The vast majority of literature work focuses on RGB images, while our specific use case is based on grayscale sinogram images from XCT. Additionally, the features of interest in our experiments may be non-existent in most of the natural world datasets.

These works focus on generating or manipulating images globally, while editing images locally R1−W1−A has received limited attention. In XCT experiments for synchrotron radiation beamlines, a small portion of whole projection is captured in a single exposure due to a limited field of view (Zhang et al., 2024), which needs to be stitched together to obtain a full projection image. In order to remove discontinuities and distortions during stitching, feature-based (Cheng et al., 2016) and cross-correlation based stitching methods (Vescovi et al., 2018) are used. However, these approaches limit the accuracy and stability of the stitched images. In XCT (especially medical applications), alpha image reconstruction (AIR) (Hofmann et al., 2014) approach is used which generates basis images based on certain properties (for example - high resolution, low noise), and subsequently generates R4−Q2−A voxel-specific weights which are applied to combine the basis images to have a final image with the desired properties. In medical Optical Coherence Tomography distortion corrections are also made with DL method (Qin et al., 2021). However, for synchrotron experiments, data types and features are diverse and data samples are limited. Blending of images, an approach which involves accurately fusing two images in local regions, has been aimed as well. Poisson image editing (Pérez et al., 2003) uses gradient driven reconstruction in pixels. Zhang et al. (2020) developed a differentiable model with Poisson loss, style loss, content loss and TV regularizer which improves the blending performance. Blended Diffusion (Avrahami et al., 2022) addresses zero-shot text-guided local image editing. Blending of outputs by optimizing the latent vector is demonstrated (Avrahami et al., 2023).

3 METHODS

3.1 PHYSICS-BASED LOSS FUNCTIONS FOR THE AUTOENCODER: The inpainting task in this paper is to recover a dense sinogram $S_d \in \mathbb{R}^{P \times Dt}$ and the corresponding reconstructed image $I_d \in \mathbb{R}^{W \times H}$ from its counterpart missing data sinogram $S_s \in \mathbb{R}^{P \times Dt}$ and its corresponding reconstructed image $I_s \in \mathbb{R}^{W \times H}$. Here, P is the number of projections, and Dt is the number of detectors. W and H are the width and height of the reconstructed object respectively. Here, we are inspired by the LDM (Rombach et al., 2022), for the task of sinogram inpainting. The autoencoder consists of a combination of perceptual loss and physics-based loss objectives derived from the principles of tomography data acquisition process. The encoder $\mathbf{E}$ takes a sparse sinogram $S_i \in \mathbb{R}^{P \times Dt}$ as input, and encodes it to a latent representation $z = \mathbf{E}(S_i)$. The sinogram S_i denotes the i th sinogram in the set of missing data sinogram S_s, thus, $S_i \subseteq S_s$. Here, the latent representation after encoding is $z \in \mathbb{R}^{w \times h \times c}$, with w and h as the width and height respectively, and c is the channels of the latent representation z. The arbitrary high variances in the latent spaces is avoided by using the Vector Quantization (VQ) layer within the decoder $\mathbf{D}$. z is quantized into z_q, and the backpropagation through the quantization operation is achieved using stop-gradient function $sg[.]$. The decoder $\mathbf{D}$ R2−Q2−A reconstructs the image from the latent representation, $\tilde{S}_i = \mathbf{D}(z_q)$. The diffusion model works with the learned latent space representation, z. The training of the autoencoder through backpropagation follows a novel loss function, which consists of domain-specific physics penalty terms derived from the Tomographic data acquisition process. The original autoencoder loss function of Esser et al. (2021), shown in Eq. 1 consists of reconstruction loss term, perceptual loss term L_P, in addition, to R1−Q1−A the codebook loss (last two terms). Here $\beta = 0.25$.

$$L_{VQ}(\mathbf{E}, \mathbf{D}, Z) = |S_i - \tilde{S}_i| + L_P + ||sg[\mathbf{E}(S_i)] - z_q||_2^2 + \beta||sg[z_q] - \mathbf{E}(S_i)||_2^2 \tag{1}$$

The autoencoder is trained in an adversarial manner using patch-based discriminator $Disc$ which differentiates the reconstructed sinogram from the actual sinogram. However, the loss formulation in Eq. 1 misses the underlying physical process of tomographic imaging. To capture the physical process of tomographic imaging, and prioritize the inpainting process for both the sinogram and object domains, we introduce additional novel physics-driven loss terms as enumerated below,

(a) Hessian penalty for Sinogram: A sinogram is a sinusoidal wave-like pattern which is piecewise linearly continuous (Xie et al., 2017). The second-order derivatives of the sinogram provide the inflection points and peaks of these sinusoids. The second-order derivatives would be very sparse (Yang et al., 2022) and are incorporated by the Hessian penalty of the function (Boyd & Vandenberghe, 2004; Sun et al., 2015; Yang et al., 2022). To capture these sparse inflection points, the Hessian penalty term L_H is introduced between reconstructed and ground truth sinograms, $\tilde{S}_i$, and $S_{i,gt}$ respectively, (Yang et al., 2022) in Eq. 2, with $\{a, b\} \in \{x, y\}$, and, $\frac{\partial^2}{\partial a \partial b} \in \{\frac{\partial^2}{\partial x^2}, \frac{\partial^2}{\partial x \partial y}, \frac{\partial^2}{\partial y \partial x}, \frac{\partial^2}{\partial y^2}\}$,

$$L_H = \sum_{x,y} \sqrt{Hs_{xx}^2 + Hs_{xy}^2 + Hs_{yx}^2 + Hs_{yy}^2} \text{with, } Hs_{ab} = \frac{\partial^2 \tilde{S}_i(a, b)}{\partial a \partial b} - \frac{\partial^2 S_{gt}(a, b)}{\partial a \partial b}. \tag{2}$$

(b) Sinogram loss for Opposite Projections: A tomographic projection sums the transmitted X-rays passing through the object which is typically rotated around the object's central axis perpendicular to the direction of X-rays. Considering parallel X-rays with the detector placed at far field, the X-rays passing through the object rotated at an angle of α radians, follows identical trajectory as for the projection, with the object rotated at an angle of $\pi + \alpha$ radians (Yang et al., 2022). In sinogram domain, the sinogram at rotation angle α radians would be identical to the sinogram at rotation angle $\pi + \alpha$ radians, flipped around the detector's central axis. We utilize this property as loss function L_O in the reconstructed sinogram as shown in Eq. 3,

$$L_O = \frac{\sum_{x,y} ||\tilde{S}_i(\alpha) - Fl_C(\tilde{S}_j)||_2^2}{P \times C}. \tag{3}$$

Here, we compute the mean error over the $P \times C$ pixels corresponding to the entire sinogram. $Fl_C(.)$ computes flipping of the sinogram with respect to the detector central axis, while we compute the difference of the reconstructed sinogram $\tilde{S}_i$ corresponding to rotation angle α, and the reconstructed sinogram $\tilde{S}_j$ corresponding to rotation angle $\alpha + \pi$.

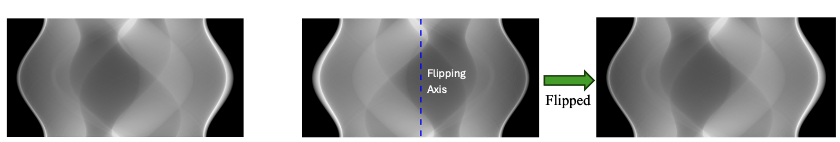

(a) Sinogram with 0 to π projection angles (b) Sinogram with π to 2π projection angles (c) Flipped Sinogram with π to 2π projection angles

Figure 3: Identical sinograms for opposite projection angles. Sinogram with π to 2π projection angles in (b) is flipped around the vertical axis to be transformed to (c), which is identical as (a).

(c) Reconstruction loss: We also match the reconstructed object by reconstructing the object from the output of the autoencoder ($\tilde{S}_i$) as well as the reconstructed object from the ground truth sinogram($S_{i,gt}$). The loss is formulated as L_{RO}, as shown in Eq. 4, where we compute the mean of the squared L_2 norm between the reconstructed object from the autoencoder ($\tilde{S}_i$) and ground truth ($S_{i,gt}$) using differentiable backprojection operator $FBP(.)$ in Eq. 4. Here W and H are the width and height of the reconstructed object. While performing sinogram to object reconstruction, a ramp filtering operation is required to remove the blurring effects . R1−Q2−A

$$L_{RO} = \frac{\sum_{x,y} ||FBP(\tilde{S}_i) - FBP(S_{i,gt})||_2^2}{W \times H}. \tag{4}$$

(d) Total Loss Function: The total loss function L_{AE} is the aggregation of the original loss function L_{VQ}, and the novel physics-driven domain losses. We weight each of these terms L_H, L_O, and, L_{RO} by k_1, k_2, and, k_3 respectively as in Eq. 5. These weights are chosen in a heuristic approach, R3−W3−A $k_1 = 10$, $k_2 = 10^3$, $k_3 = 10^5$ such that the contribution from each of these loss terms is equal. The R4−Q6−A autoencoder is trained in an adversarial manner for the sinogram inpainting task.

$$L_{AE} = L_{VQ} + k_1 L_H + k_2 L_O + k_3 L_{RO} \tag{5}$$

Overall, the addition of these physics-based penalty terms introduces stability during the training of the Autoencoder. These losses also reduce the differences between the reconstructions and the ground truths in both the sinogram and reconstruction domains.

3.2 DIFFUSION MODEL AND BLENDING: The diffusion model of the LDM models the conditional distribution $p(z|y)$ with inputs y as the condition. In this work, we use the masks as the conditional input y. The mask y is downsampled and concatenated to the encoded masked sinogram, and mapped to intermediate layers of the U-Net using a cross-attention mechanism, which is defined as, $Attention(Q, K, V) = softmax(QK^T/\sqrt{d}).V$, with query Q, key K, and value V containing trainable projection matrices. Based on the image-conditioning mask pairs, the conditional LDM is learned using the loss function in Eq. 6 with, ϵ_θ is the neural backbone of the diffusion model, realized by U-Net model, and z_t is the input latent representation of the tth equal sequence in the denoising U-Net, with $t = 1, ..., T$.

$$L_{LDM,inpaint} = \mathbb{E}_{\mathbf{E}(x),y\sim N(0,1),t}[||\epsilon - \epsilon_\theta(z_t, t, \tau_\theta(y))||_2^2]. \tag{6}$$

In the inpainting problem, given a missing data sinogram S_s (Fig. 4(a)) and a binary mask m corresponding to the missing regions, the LDM outputs a dense sinogram $\hat{S}_d$. Information from the sinograms S_s and $\hat{S}_d$ is combined to form the final blended sinogram as $S_d = \hat{S}_d \odot m + S_s \odot (1 - m)$, as shown in Fig. 4(b), as the copy-paste sinogram, with $\odot$ being described as the element-wise product. The straightforward approach of combining the background and foreground objects by directly copying a foreground object from the source (inpainted) image and pasting it to the background object from the target image causes big intensity changes at the boundaries, creating artifacts visible to the human eye, as shown in Fig. 4(b). We blend the information from the foreground to that of the background in a novel approach, which minimizes the artifacts as illustrated in Fig. 4(c), compared to the actual sinogram shown in Fig. 4(d). We perform an optimization over the latent vector z_0 as a post-processing step to search for an optimal vector z^* so that the masked area is similar to the edited image $\hat{S}_d$, and the unmasked region is similar to the input image S_s. This is shown in Eq. 7, where the sum of the mean squared error loss is computed between the edited image $\hat{S}_d$ and the decoder output for the masked region m, and the corresponding sparse image S_s and the decoder output for the unmasked regions $1 - m$. The factor γ preserves the fidelity to the background region S_s ($\gamma = 1000$ used in our experiments).

$$L_{fid} = \frac{1}{N_{pixs}} \sum_{x,y} \left\{ (\mathbf{D}(z) \odot m - \hat{S}_d \odot m)^2 + \gamma(\mathbf{D}(z) \odot (1 - m) - S_s \odot (1 - m))^2 \right\} \tag{7}$$

Additional style loss and TV regularization are introduced in the optimization. The TV regularization loss drives the latent vector to remove the high-frequency noise. The style loss (L_{style}) aims to preserve the style of the input masked sinogram S_s and the output sinogram $\hat{S}_{d1}$, as in Eq. 8.

$$L_{style} = \sum_{l=1}^{L} \frac{\beta_l}{2N_l^2} \sum_{i=1}^{N_l} \sum_{j=1}^{N_l} (G_l[S_d] - G_l[\mathbf{D}(z^*)]])_{ij}^2 \tag{8}$$

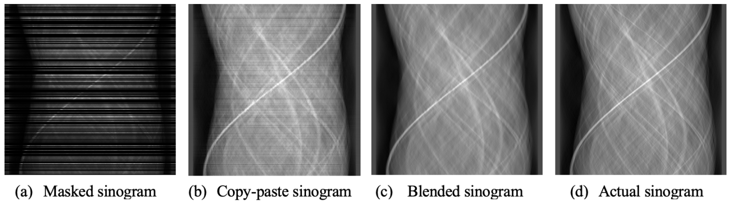

Figure 4: Randomly masked sinogram and its inpainting approaches.

In Eq. 8, $\mathbf{D}$ is the decoder of the autoencoder in the LDM, L is the number of convolutional layers, N_l is the number of channels in activation, M_l is the number of flattened activation values in each channel. $F_l[.] \in \mathbb{R}^{N_l \times M_l}$ is an activation matrix computed from a deep network F at the l^{th} layer. $G_l[.] = F_l[.]F_l[.]^T \in \mathbb{R}^{N_l \times N_l}$ denotes the Gram matrix of the corresponding activation at the l^{th} layer which captures similarity relation between all pairs of channels that encode image style and texture. The weights β_l control the influence of each layer. The TV loss (L_{TV}) is defined as Eq. 9.

$$L_{TV} = \sum_{m=1}^{H} \sum_{n=1}^{W} |\mathbf{D}(z^*)(m+1,n) - \mathbf{D}(z^*)(m,n)| + |\mathbf{D}(z^*)(m,n+1) - \mathbf{D}(z^*)(m,n)| \tag{9}$$

The total blending loss is defined as L_{blend} in Eq. 10 with the multiplicative factors p_{fid}, p_s, p_{TV} corresponding to the L_{fid}, L_{style} and L_{TV} respectively. In our experiments, $p_{fid} = 1$, $p_s = 10^4$, R4−Q6−A and, $p_{TV} = 10^{-6}$ is used such that the fidelity loss has higher contribution in the overall loss. The R3−W3−A loss L_{blend} is optimized for each image, with no separate training stage.

$$L_{blend} = p_{fid} L_{fid} + p_s L_{style} + p_{TV} L_{TV} \tag{10}$$

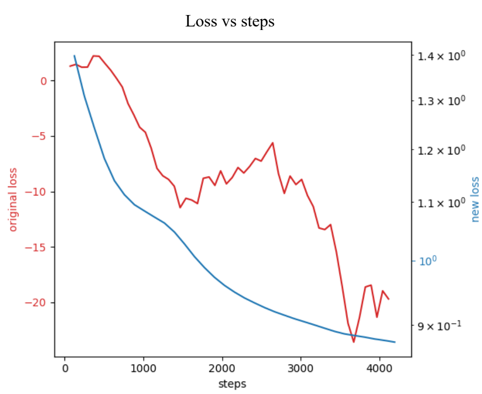

Table 1: Performance of **Autoencoder** trained with different loss settings

AutoEncoder	Sinogram		Reconstruction	
	SSIM	PSNR (dB)	SSIM	PSNR (dB)
Org loss	0.9429	38.18	0.8571	35.64
New loss	**0.9602**	**38.83**	**0.8944**	**37.42**
New loss w/o L_O	0.9590	38.84	0.8954	37.20
New loss w/o L_O and L_H	0.9544	37.79	0.8891	36.98

Table 2: Performance of **Autoencoder** trained with **New loss** for different training data

Training Dataset	Sinogram		Reconstruction	
	SSIM	PSNR (dB)	SSIM	PSNR (dB)
Real World	**0.9602**	**38.83**	**0.8944**	**37.42**
Real World + Phantom (Shapes)	0.9400	33.95	0.8765	36.11
Phantom (Shapes)	0.6845	16.83	0.6290	29.16

Figure 5: Left: training loss over steps. Blue curve - autoencoder trained with new loss; red curve - R2−W1−A autoencoder trained with the original loss. Table 1 shows the autoencoder performance at different R2−W2−A loss settings . Table 2 shows the autoencoder performance trained with different data distributions. R3−W2−A

4 Experimental Results

The real-world data is curated from the XCT data present in TomoBank repository by De Carlo R2−W2−A et al. (2018) based on feature complexity and contrast, alongwith the quality of sinogram and reconstruction images, which is termed as Exp_Data. We emphasize that collecting this real-world data from experiments at synchrotron beamlines is laborious and difficult to obtain. Sinogram data corresponding to the tomo_IDs of $1-4$, $23-26$, $31-56$, $64-75$, 77, 82, 85, 88, $90-93$, 96, 104, 107, 110 have been selected. More details about the dataset can be found in TomoBank webpage. R4−Q3−A The image resolution is different based on the corresponding experiments. In order to train and evaluate the DL model, we obtain a common image resolution size of 512×512 by performing data pre-processing in a step-wise manner. First, from the original projections, we reconstruct the object. Second, we reshape the object to a predefined shape and re-project the object to the desired rotation angles. Subsequently, the re-projections are converted to sinograms by transposing the projection angle axis with the x axis of the projection image. This curated dataset falls in the realm of "small dataset", especially when compared to datasets with millions of images used for training foundation models, often used in literature. For training the autoencoder and diffusion model in the LDM, we use 50,000 training data, and 12,500 validation data randomly selected from Exp_Data. For comparing the autoencoder performance with different data distributions, the autoencoder is also trained with real-world data augmented with synthetic phantom data composed of simple shapes - circles, triangles, and polygons as shown in Table 2. The total training and validation data size is same in all the cases. R3−Q3−A The autoencoder is trained with the loss function L_{AE} as shown in Eq. 5 for 4,000 steps. We use original unmasked sinograms to train the autoencoder, while for training the diffusion model, randomly masked sinograms with mask ratio varying between $0.1 - 0.9$ are used along with the binary masked regions during the pre-training stage. The pre-training of the diffusion model in the LDM has been done for 3,500 steps. For fine-tuning the diffusion model to different downstream tasks such as inpainting the SV and LA problems, the model utilizes fewer data, using 25,000 training data and 6,250 validation data selected randomly from Exp_Data. This fine-tuning do not require a high computational overload and can be implemented on a single compute node with upto 4 GPUs . R1−Q3−A We analyze the performance with 50 real-world test data samples that consist of simple and complex features. We used Polaris supercomputer and Lambda cluster at Argonne Leadership Computing Facility for model training and testing. Polaris supercomputer consists of 560 compute nodes, each having 4 NVIDIA A100 GPUs connected via NVLink. Lambda nodes, on the other hand, are DGX-1 machines that consist of 8 NVIDIA V100 GPUs each. We use Pytorch version 2.3.0 and CUDA version 12.4. Depending on the number of GPUs used during the training of the model, the learning rate (lr) can be defined as, $lr = lr_{base} \times grad\,accum\,steps \times GPU\,num \times batch\,size$. The training time for the autoencoder (stage-1) is 4 days using 6 NVIDIA V100 GPUs, while for pre-training the Diffusion Model (stage-2) takes 3 days, and, fine-tuning for the downstream tasks, the training time is 2 days - both using 4 NVIDIA V100 GPUs. R2−Q1−A The inference time for inpainting with the diffusion model is 9.23 seconds per image for 50 sampling steps in one NVIDIA V100 GPU. On the same hardware resource, the blending stage (stage - 3) is an iterative process that takes 0.69 seconds/iteration. Convergence of the blending algorithm is observed after 35 iteration steps.

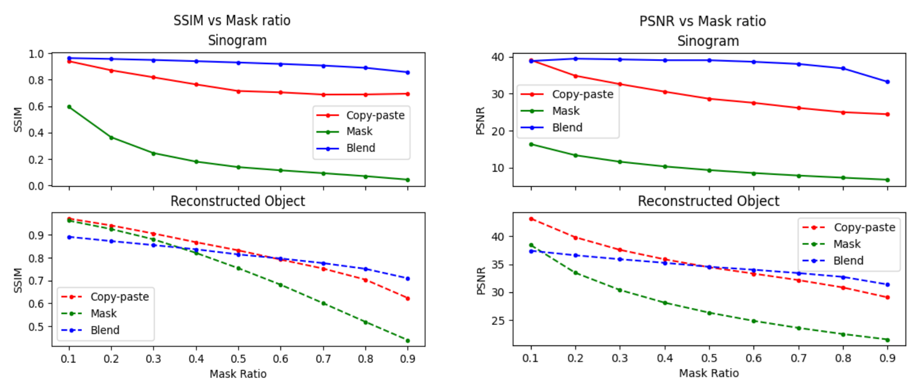

R1−W2−A
R3−W4−A

Figure 6: SSIM (left) and PSNR (right) vs mask ratio for sinogram (top) and reconstruction (bottom).

4.1 Training and Performance of Autoencoder

The autoencoder training is critical for the success of this model. We emphasize that training the autoencoder with additional physics losses aids in its stable training along with the improvement of the autoencoder's performance. Fig. 5 shows the training loss with and without the additional physics-based loss terms, which are the blue and red curves respectively. It is evident that the red curve oscillates a lot, while the blue curve converges smoothly during the training of the autoencoder. Table 1 shows the SSIM and PSNR performance of the autoencoder with various loss configura-

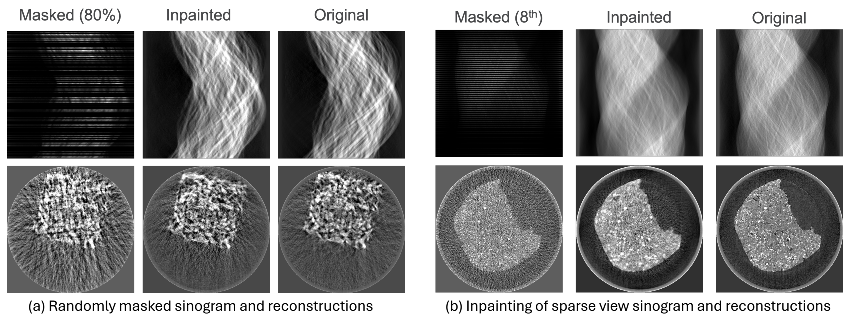

Figure 7: Inpainting of (a) 80% randomly masked sinogram (top), and, (b) SV sinogram (every 8th projection acquired) (top), and its reconstructions (bottom). R1–W2–A R2–Q4–A R4–Q4–A

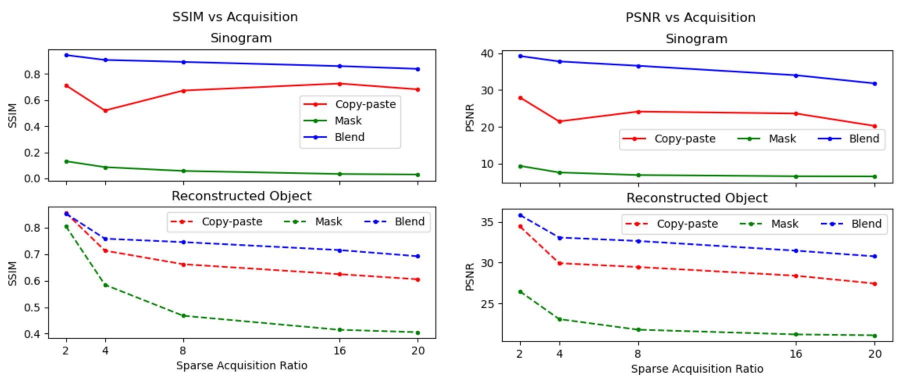

Figure 8: SSIM (left) and PSNR (right) vs SV acquisition for sinogram and reconstruction. R1–W2–A

tions. We observe that the autoencoder trained with L_{AE} performs best across the sinogram and reconstructed object domain. In Table 2, we demonstrate that combining the real-world data with synthetic data in $50:50$ ratio captures a wide range of features and performs close to the autoencoder trained with real-world data, while the one trained with only synthetic data performs worst.

4.2 Performance for Randomly Masked Data

Fig. 6 (left and right respectively) shows the variation of SSIM and PSNR over the mask ratio for the inpainted sinograms as well as for the reconstructed object obtained from these inpainted sinograms. In the sinogram domain (top row), the blending of the model's prediction with that of the unmasked sinogram indeed improves the performance, as seen by the blue and red solid plots. In the reconstructed object domain (bottom row), it is seen that the reconstruction from the sinogram with the masked region copied from the prediction and pasted to the unmasked region of the input sinogram produces better SSIM compared to the blended reconstructed object for lower mask ratios (< 0.5). This can be attributed to the TV loss introduced in the blending, which promotes smoother solutions. However, for higher mask ratios, the blended object performs better than the reconstruction from the copy-paste sinogram. For reconstructions from masked sinograms, it is observed that the SSIM is quite high for smaller mask ratios (< 0.3), which drops with the increase in mask ratio. With very sparse data (mask ratio ~ 0.9), the SSIM of reconstruction from the masked sinogram is the worst. The PSNR vs mask ratio plots (right column in Fig. 6) has similar trends as in the SSIM vs mask ratio plots (left column in Fig. 6). Fig. 7 (a) shows an example of real-world sinogram inpainting (top row) with 80% of its data missing, and its reconstructions (bottom row). The PSNR values of the sinograms as well as the reconstructed object for the blended output surpass the copy-paste (sinogram and reconstructions) and mask reconstruction metrics. Overall, the trends of SSIM and PSNR over mask ratio are identical.

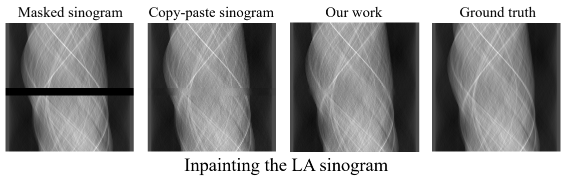

Table 3: Performance (LA only) of our model for inpainting of LA Problem

Methods	Sinogram					
	Missing Angle (degrees)					
	10		20		30	
	SSIM	PSNR (dB)	SSIM	PSNR (dB)	SSIM	PSNR (dB)
Copy-paste	0.7395	26.74	0.7393	26.92	0.7067	25.47
Blended	**0.7793**	**33.08**	**0.7681**	**31.81**	**0.7387**	**30.71**

Figure 9: Left: Inpainting the LA sinogram. Table 3 shows performance for LA problem.

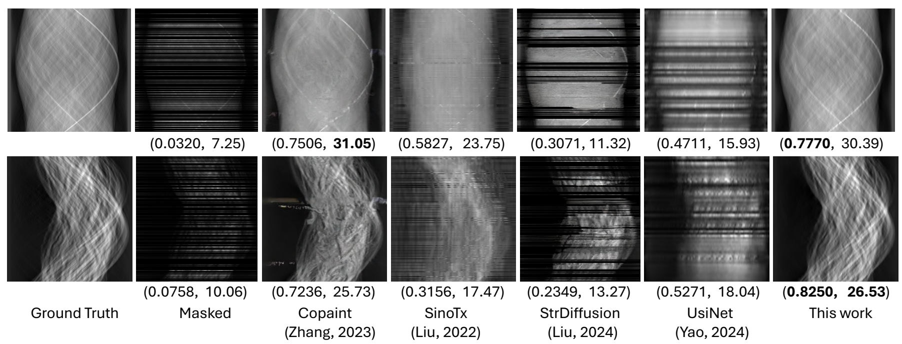

Figure 10: Inpainting performance comparison of our model with other state-of-art techniques for 80% random masking. (SSIM, PSNR) values provided at the bottom of each row. R1−W2−A R4−Q5−A

4.3 Performance for Downstream Tasks and Baseline Comparisons

SV Acquisition: Inpainting in the realm of SV data is one of the downstream task after pre-training. Fig. 7 (b) shows the SV sinogram with the data acquired for every 8th sample and its inpainting (top row), and the reconstructed object (bottom row). Fig. 8 shows the inpainting of the SV data with the SSIM metrics in the sinogram (top left) and the reconstructed object domains (bottom left). The blended sinogram (blue solid) exceeds the copy-pasted sinogram (red solid) for all the sparse ratios. Additionally, the reconstructed object from the blended sinogram (blue dashed) plot surpasses the reconstructed object from the unmasked regions of the sinogram (green dashed plot), as well as the copy-pasted sinogram (red dashed plot). Identical trends are observed with the PSNR metrics as well as shown in Fig. 8(right). For all sparse ratios, the PSNR for the blended sinogram (blue solid), as well as the reconstructed object (blue dashed) from the blended sinogram, is maximum.

Performance for LA Problem: Inpainting of the LA problem is another downstream task, which involves the inpainting of a bigger mask region. Fig. 9 (left) shows a sample performance of our model, while Table 3 shows the SSIM and PSNR metrics for inpainted and copy-paste sinogram. Clearly, the blended sinogram outperforms the copy-paste sinogram based on these metrics.

Baseline Comparisons: In order to obtain a fair comparison with other state-of-art algorithms, we compare our work with other inpainting approaches such as Copaint (Zhang et al., 2023), SinoTx (Liu et al., 2022), StrDiffusion (Liu et al., 2024), UsiNet (Yao et al., 2024) . Fig. 10 shows the comparative performance. We can see significant artifacts being present in inpainting from SinoTx and Copaint. StrDiffusion and UsiNet contains horizontal dark stripes which is erroneous. We demonstrate our model as the best performing one with CoPaint performing closely, but with artifacts. R1−W1−A

5 Conclusion

This paper presents a novel method combining domain-specific physics knowledge with the SDM for inpainting in the sinogram domain from real-world CT experimental data. It introduces the physics loss functions in the sinogram as well as in the reconstructed object domains and a novel blending algorithm. It develops a foundation model pre-trained on random masking and fine tunes it on tasks such as sparsely acquired data and missing wedge problems. Our model outperforms the state-of-the-art baselines by 23.5% for sinogram and 13.8% reconstructed object in terms of SSIM.

REFERENCES

Amogh Subbakrishna Adishesha, Daniel J Vanselow, Patrick La Riviere, Keith C Cheng, and Sharon X Huang. Sinogram domain angular upsampling of sparse-view micro-ct with dense residual hierarchical transformer and attention-weighted loss. *Computer Methods and Programs in Biomedicine*, 242:107802, 2023.

Jonas Adler and Ozan Öktem. Solving ill-posed inverse problems using iterative deep neural networks. *Inverse Problems*, 33(12):124007, 2017.

Advanced Photon Source, Argonne National Laboratory. Research and Engineering Highlights. `https://www.aps.anl.gov/APS-Science-Highlight/All`. [Accessed: Sept. 2024].

Anders H Andersen and Avinash C Kak. Simultaneous algebraic reconstruction technique (sart): a superior implementation of the art algorithm. *Ultrasonic imaging*, 6(1):81–94, 1984.

Omri Avrahami, Dani Lischinski, and Ohad Fried. Blended diffusion for text-driven editing of natural images. In *Proceedings of the IEEE/CVF conference on computer vision and pattern recognition*, pp. 18208–18218, 2022.

Omri Avrahami, Ohad Fried, and Dani Lischinski. Blended latent diffusion. *ACM transactions on graphics (TOG)*, 42(4):1–11, 2023.

Kees Joost Batenburg and Jan Sijbers. Dart: a practical reconstruction algorithm for discrete tomography. *IEEE Transactions on Image Processing*, 20(9):2542–2553, 2011.

SP Boyd and L Vandenberghe. Sec. 9.2: Descent methods. *Convex Optimization. Cambridge University Press, Cambridge, UK; New York*, 2004.

Chang-Chieh Cheng, Yeukuang Hwu, and Yu-Tai Ching. High-resolution and large-volume tomography reconstruction for x-ray microscopy. In *Medical Imaging 2016: Physics of Medical Imaging*, volume 9783, pp. 1251–1257. SPIE, 2016.

Francesco De Carlo, Doğa Gürsoy, Daniel J Ching, K Joost Batenburg, Wolfgang Ludwig, Lucia Mancini, Federica Marone, Rajmund Mokso, Daniël M Pelt, Jan Sijbers, et al. Tomobank: a tomographic data repository for computational x-ray science. *Measurement Science and Technology*, 29(3):034004, 2018.

Ye Deng, Siqi Hui, Rongye Meng, Sanping Zhou, and Jinjun Wang. Hourglass attention network for image inpainting. In *European conference on computer vision*, pp. 483–501. Springer, 2022.

Qiaoqiao Ding, Hui Ji, Hao Gao, and Xiaoqun Zhang. Learnable multi-scale fourier interpolation for sparse view ct image reconstruction. In *Medical Image Computing and Computer Assisted Intervention–MICCAI 2021: 24th International Conference, Strasbourg, France, September 27–October 1, 2021, Proceedings, Part VI 24*, pp. 286–295. Springer, 2021.

Xu Dong, Swapnil Vekhande, and Guohua Cao. Sinogram interpolation for sparse-view micro-ct with deep learning neural network. In *Medical Imaging 2019: Physics of Medical Imaging*, volume 10948, pp. 692–698. SPIE, 2019.

Alexey Dosovitskiy, Lucas Beyer, Alexander Kolesnikov, Dirk Weissenborn, Xiaohua Zhai, Thomas Unterthiner, Mostafa Dehghani, Matthias Minderer, Georg Heigold, Sylvain Gelly, et al. An image is worth 16x16 words: Transformers for image recognition at scale. *arXiv preprint arXiv:2010.11929*, 2020.

Betsy A Dowd, Graham H Campbell, Robert B Marr, Vivek V Nagarkar, Sameer V Tipnis, Lisa Axe, and D Peter Siddons. Developments in synchrotron x-ray computed microtomography at the national synchrotron light source. In *Developments in X-ray Tomography II*, volume 3772, pp. 224–236. SPIE, 1999.

Eva L Dyer, William Gray Roncal, Judy A Prasad, Hugo L Fernandes, Doga Gürsoy, Vincent De Andrade, Kamel Fezzaa, Xianghui Xiao, Joshua T Vogelstein, Chris Jacobsen, et al. Quantifying mesoscale neuroanatomy using x-ray microtomography. *eneuro*, 4(5), 2017.

Jiaze E, Srutarshi Banerjee, Tekin Bicer, Guannan Wang, and Bin Ren. Fcdm: Sparse-view sinogram inpainting with frequency domain convolution enhanced diffusion models. 2024. URL `https://api.semanticscholar.org/CorpusID:272593134`.

Patrick Esser, Robin Rombach, and Bjorn Ommer. Taming transformers for high-resolution image synthesis. In *Proceedings of the IEEE/CVF conference on computer vision and pattern recognition*, pp. 12873–12883, 2021.

Muhammad Usman Ghani and W Clem Karl. Deep learning-based sinogram completion for low-dose ct. In *2018 IEEE 13th Image, Video, and Multidimensional Signal Processing Workshop (IVMSP)*, pp. 1–5. IEEE, 2018.

Peter Gilbert. Iterative methods for the three-dimensional reconstruction of an object from projections. *Journal of theoretical biology*, 36(1):105–117, 1972.

Ian Goodfellow, Jean Pouget-Abadie, Mehdi Mirza, Bing Xu, David Warde-Farley, Sherjil Ozair, Aaron Courville, and Yoshua Bengio. Generative adversarial nets. *Advances in neural information processing systems*, 27, 2014.

Wei He, Quanming Yao, Chao Li, Naoto Yokoya, and Qibin Zhao. Non-local meets global: An integrated paradigm for hyperspectral denoising. In *Proceedings of the IEEE/CVF Conference on Computer Vision and Pattern Recognition*, pp. 6868–6877, 2019.

Gabor T Herman and Arnold Lent. Iterative reconstruction algorithms. *Computers in biology and medicine*, 6(4):273–294, 1976a.

Gabor T Herman and Arnold Lent. Quadratic optimization for image reconstruction. i. *Computer Graphics and Image Processing*, 5(3):319–332, 1976b.

Christian Hofmann, Stefan Sawall, Michael Knaup, and Marc Kachelrieß. Alpha image reconstruction (air): a new iterative ct image reconstruction approach using voxel-wise alpha blending. *Medical physics*, 41(6Part1):061914, 2014.

Intelligence Advanced Research Projects Activity. Rapid Analysis of Various Emerging Nanoelectronics. `https://www.iarpa.gov/index.php/research-programs/raven`. [Accessed: Oct. 2023].

Avinash C Kak and Malcolm Slaney. *Principles of computerized tomographic imaging*. SIAM, 2001.

Ulugbek S Kamilov, Charles A Bouman, Gregery T Buzzard, and Brendt Wohlberg. Plug-and-play methods for integrating physical and learned models in computational imaging: Theory, algorithms, and applications. *IEEE Signal Processing Magazine*, 40(1):85–97, 2023.

Kleoniki Keklikoglou, Christos Arvanitidis, Georgios Chatzigeorgiou, Eva Chatzinikolaou, Efstratios Karagiannidis, Triantafyllia Koletsa, Antonios Magoulas, Konstantinos Makris, George Mavrothalassitis, Eleni-Dimitra Papanagnou, et al. Micro-ct for biological and biomedical studies: a comparison of imaging techniques. *Journal of imaging*, 7(9):172, 2021.

Keunsoo Ko and Chang-Su Kim. Continuously masked transformer for image inpainting. In *Proceedings of the IEEE/CVF International Conference on Computer Vision*, pp. 13169–13178, 2023.

Andreas Kofler, Markus Haltmeier, Christoph Kolbitsch, Marc Kachelrieß, and Marc Dewey. A u-nets cascade for sparse view computed tomography. In *Machine Learning for Medical Image Reconstruction: First International Workshop, MLMIR 2018, Held in Conjunction with MICCAI 2018, Granada, Spain, September 16, 2018, Proceedings 1*, pp. 91–99. Springer, 2018.

Hiroyuki Kudo, Taizo Suzuki, and Essam A Rashed. Image reconstruction for sparse-view ct and interior ct—introduction to compressed sensing and differentiated backprojection. *Quantitative imaging in medicine and surgery*, 3(3):147, 2013.

Hoyeon Lee, Jongha Lee, Hyeongseok Kim, Byungchul Cho, and Seungryong Cho. Deep-neural-network-based sinogram synthesis for sparse-view ct image reconstruction. *IEEE Transactions on Radiation and Plasma Medical Sciences*, 3(2):109–119, 2018.

Xiaoguang Li, Qing Guo, Di Lin, Ping Li, Wei Feng, and Song Wang. Misf: Multi-level interactive siamese filtering for high-fidelity image inpainting. In *Proceedings of the IEEE/CVF conference on computer vision and pattern recognition*, pp. 1869–1878, 2022.

Wei-An Lin, Haofu Liao, Cheng Peng, Xiaohang Sun, Jingdan Zhang, Jiebo Luo, Rama Chellappa, and Shaohua Kevin Zhou. Dudonet: Dual domain network for ct metal artifact reduction. In *Proceedings of the IEEE/CVF Conference on Computer Vision and Pattern Recognition*, pp. 10512–10521, 2019.

Haipeng Liu, Yang Wang, Biao Qian, Meng Wang, and Yong Rui. Structure matters: Tackling the semantic discrepancy in diffusion models for image inpainting. In *Proceedings of the IEEE/CVF Conference on Computer Vision and Pattern Recognition*, pp. 8038–8047, 2024.

Zhengchun Liu, Tekin Bicer, Rajkumar Kettimuthu, Doga Gursoy, Francesco De Carlo, and Ian Foster. Tomogan: low-dose synchrotron x-ray tomography with generative adversarial networks: discussion. *JOSA A*, 37(3):422–434, 2020.

Zhengchun Liu, Rajkumar Kettimuthu, and Ian Foster. Masked sinogram model with transformer for ill-posed computed tomography reconstruction: a preliminary study. *arXiv preprint arXiv:2209.01356*, 2022.

Andreas Lugmayr, Martin Danelljan, Andres Romero, Fisher Yu, Radu Timofte, and Luc Van Gool. Repaint: Inpainting using denoising diffusion probabilistic models. In *Proceedings of the IEEE/CVF conference on computer vision and pattern recognition*, pp. 11461–11471, 2022.

Patrick Pérez, Michel Gangnet, and Andrew Blake. Poisson image editing. In *Seminal Graphics Papers: Pushing the Boundaries, Volume 2*, pp. 577–582. 2003.

Guohong Qin, Congrui Yang, and Yixin Du. Image enhancement of optical coherence tomography using deep learning. In *2021 IEEE International Conference on Artificial Intelligence and Industrial Design (AIID)*, pp. 217–221. IEEE, 2021.

Mark L Rivers. tomorecon: High-speed tomography reconstruction on workstations using multi-threading. In *Developments in X-ray tomography VIII*, volume 8506, pp. 169–181. SPIE, 2012.

Robin Rombach, Andreas Blattmann, Dominik Lorenz, Patrick Esser, and Björn Ommer. High-resolution image synthesis with latent diffusion models. In *Proceedings of the IEEE/CVF conference on computer vision and pattern recognition*, pp. 10684–10695, 2022.

Olaf Ronneberger, Philipp Fischer, and Thomas Brox. U-net: Convolutional networks for biomedical image segmentation. In *Medical image computing and computer-assisted intervention–MICCAI 2015: 18th international conference, Munich, Germany, October 5-9, 2015, proceedings, part III 18*, pp. 234–241. Springer, 2015.

Pooria Sedigh Rahimabadi, Mehdi Khodaei, and Kaveenga R Koswattage. Review on applications of synchrotron-based x-ray techniques in materials characterization. *X-Ray Spectrometry*, 49(3): 348–373, 2020.

Emil Y Sidky and Xiaochuan Pan. Image reconstruction in circular cone-beam computed tomography by constrained, total-variation minimization. *Physics in Medicine & Biology*, 53(17):4777, 2008.

Tao Sun, Nanbo Sun, Jing Wang, and Shan Tan. Iterative cbct reconstruction using hessian penalty. *Physics in Medicine & Biology*, 60(5):1965, 2015.

Roman Suvorov, Elizaveta Logacheva, Anton Mashikhin, Anastasia Remizova, Arsenii Ashukha, Aleksei Silvestrov, Naejin Kong, Harshith Goka, Kiwoong Park, and Victor Lempitsky. Resolution-robust large mask inpainting with fourier convolutions. In *Proceedings of the IEEE/CVF winter conference on applications of computer vision*, pp. 2149–2159, 2022.

Jiaxing Tan, Yongfeng Gao, Yumei Huo, Lihong Li, and Zhengrong Liang. Sharpness preserved sinogram synthesis using convolutional neural network for sparse-view ct imaging. In *Medical Imaging 2019: Image Processing*, volume 10949, pp. 102–109. SPIE, 2019.

Fengcheng Tang, Zhibin Wu, Chao Yang, Markus Osenberg, André Hilger, Kang Dong, Henning Markötter, Ingo Manke, Fu Sun, Libao Chen, et al. Synchrotron x-ray tomography for rechargeable battery research: fundamentals, setups and applications. *Small Methods*, 5(9):2100557, 2021.

Emilien Valat, Katayoun Farrahi, and Thomas Blumensath. Sinogram inpainting with generative adversarial networks and shape priors. *Tomography*, 9(3):1137–1152, 2023.

A Van der Sluis and HA Van der Vorst. Sirt-and cg-type methods for the iterative solution of sparse linear least-squares problems. *Linear Algebra and its Applications*, 130:257–303, 1990.

Bert Vandeghinste, Bart Goossens, Jan De Beenhouwer, Aleksandra Pizurica, Wilfried Philips, Stefaan Vandenberghe, and Steven Staelens. Split-bregman-based sparse-view ct reconstruction. In *11th International meeting on Fully Three-Dimensional Image Reconstruction in Radiology and Nuclear Medicine (Fully 3D 11)*, pp. 431–434, 2011.

Singanallur V Venkatakrishnan, Lawrence F Drummy, Michael Jackson, Marc De Graef, Jeff Simmons, and Charles A Bouman. Model-based iterative reconstruction for bright-field electron tomography. *IEEE Transactions on Computational Imaging*, 1(1):1–15, 2014.

Rafael Vescovi, Ming Du, V de Andrade, William Scullin, Doğa Gürsoy, and Chris Jacobsen. Tomosaic: efficient acquisition and reconstruction of teravoxel tomography data using limited-size synchrotron x-ray beams. *Journal of synchrotron radiation*, 25(5):1478–1489, 2018.

Jiaxi Wang, Li Zeng, Chengxiang Wang, and Yumeng Guo. Admm-based deep reconstruction for limited-angle ct. *Physics in Medicine & Biology*, 64(11):115011, 2019.

Sukai Wang, Xuan Li, and Ping Chen. Admm-svnet: An admm-based sparse-view ct reconstruction network. In *Photonics*, volume 9, pp. 186. MDPI, 2022.

Tao Wang, Wenjun Xia, Jingfeng Lu, and Yi Zhang. A review of deep learning ct reconstruction from incomplete projection data. *IEEE Transactions on Radiation and Plasma Medical Sciences*, 2023.

Haoyu Wei, Florian Schiffers, Tobias Würfl, Daming Shen, Daniel Kim, Aggelos K Katsaggelos, and Oliver Cossairt. 2-step sparse-view ct reconstruction with a domain-specific perceptual network. *arXiv preprint arXiv:2012.04743*, 2020.

Weiwen Wu, Dianlin Hu, Chuang Niu, Hengyong Yu, Varut Vardhanabhuti, and Ge Wang. Drone: Dual-domain residual-based optimization network for sparse-view ct reconstruction. *IEEE Transactions on Medical Imaging*, 40(11):3002–3014, 2021.

Ziling Wu, Tekin Bicer, Zhengchun Liu, Vincent De Andrade, Yunhui Zhu, and Ian T Foster. Deep learning-based low-dose tomography reconstruction with hybrid-dose measurements. In *2020 IEEE/ACM Workshop on Machine Learning in High Performance Computing Environments (MLHPC) and Workshop on Artificial Intelligence and Machine Learning for Scientific Applications (AI4S)*, pp. 88–95. IEEE, 2020.

Tobias Würfl, Florin C Ghesu, Vincent Christlein, and Andreas Maier. Deep learning computed tomography. In *Medical Image Computing and Computer-Assisted Intervention-MICCAI 2016: 19th International Conference, Athens, Greece, October 17-21, 2016, Proceedings, Part III 19*, pp. 432–440. Springer, 2016.

Qi Xie, Dong Zeng, Qian Zhao, Deyu Meng, Zongben Xu, Zhengrong Liang, and Jianhua Ma. Robust low-dose ct sinogram preprocessing via exploiting noise-generating mechanism. *IEEE transactions on medical imaging*, 36(12):2487–2498, 2017.

Liutao Yang, Zhongnian Li, Rongjun Ge, Junyong Zhao, Haipeng Si, and Daoqiang Zhang. Low-dose ct denoising via sinogram inner-structure transformer. *IEEE transactions on medical imaging*, 42(4):910–921, 2022.

Lehan Yao, Zhiheng Lyu, Jiahui Li, and Qian Chen. No ground truth needed: unsupervised sinogram inpainting for nanoparticle electron tomography (usinet) to correct missing wedges. *npj Computational Materials*, 10(1):28, 2024.

Dong Hye Ye, Somesh Srivastava, Jean-Baptiste Thibault, Ken Sauer, and Charles Bouman. Deep residual learning for model-based iterative ct reconstruction using plug-and-play framework. In *2018 IEEE International Conference on Acoustics, Speech and Signal Processing (ICASSP)*, pp. 6668–6672. IEEE, 2018.

Seunghwan Yoo, Xiaogang Yang, Mark Wolfman, Doga Gursoy, and Aggelos K Katsaggelos. Sinogram image completion for limited angle tomography with generative adversarial networks. In *2019 IEEE International Conference on Image Processing (ICIP)*, pp. 1252–1256. IEEE, 2019.

Xiaobo Zhai, Dongsheng Lei, Meng Zhang, Jianfang Liu, Hao Wu, Yadong Yu, Lei Zhang, and Gang Ren. Lottor: an algorithm for missing-wedge correction of the low-tilt tomographic 3d reconstruction of a single-molecule structure. *Scientific reports*, 10(1):10489, 2020.

Guanhua Zhang, Jiabao Ji, Yang Zhang, Mo Yu, Tommi S Jaakkola, and Shiyu Chang. Towards coherent image inpainting using denoising diffusion implicit models. 2023.

Lingzhi Zhang, Tarmily Wen, and Jianbo Shi. Deep image blending. In *Proceedings of the IEEE/CVF winter conference on applications of computer vision*, pp. 231–240, 2020.

Zhen Zhang, Chun Li, Wenhui Wang, Zheng Dong, Gongfa Liu, Yuhui Dong, and Yi Zhang. Towards full-stack deep learning-empowered data processing pipeline for synchrotron tomography experiments. *The Innovation*, 5(1), 2024.

Chen Zhao, Chuanwei Wang, Xiang Liu, Inhui Hwang, Tianyi Li, Xinwei Zhou, Jiecheng Diao, Junjing Deng, Yan Qin, Zhenzhen Yang, et al. Suppressing strain propagation in ultrahigh-ni cathodes during fast charging via epitaxial entropy-assisted coating. *Nature Energy*, pp. 1–12, 2024.

Ji Zhao, Zhiqiang Chen, Li Zhang, and Xin Jin. Unsupervised learnable sinogram inpainting network (sin) for limited angle ct reconstruction. *arXiv preprint arXiv:1811.03911*, 2018.

Zangen Zhu, Khan Wahid, Paul Babyn, David Cooper, Isaac Pratt, and Yasmin Carter. Improved compressed sensing-based algorithm for sparse-view ct image reconstruction. *Computational and mathematical methods in medicine*, 2013(1):185750, 2013.